

Article

High Performance Multilayered Organosilicon/Silicon Oxynitride Water Barrier Structure Consecutively Deposited by Plasma-Enhanced Chemical Vapor Deposition at a Low-Temperature

Ren-Da Fu ¹, Che Kai Chang ¹, Ming-Yueh Chuang ², Tai-Hong Chen ³, Shao-Kai Lu ¹ and Day-Shan Liu ^{1,*}

¹ Institute of Electro-Optical and Material Science, National Formosa University, Yunlin 640, Taiwan; 40326133@gm.nfu.edu.tw (R.-D.F.); 40426123@gm.nfu.edu.tw (C.K.C.); eric0916a@gmail.com (S.-K.L.)

² Research and Development Center, Creating Nano Technologies, Tainan 700, Taiwan; a0922639175@gmail.com

³ Additive Manufacturing and Laser Application, Industrial Technology Research Institute, Tainan 700, Taiwan; thchen1208@itri.org.tw

* Correspondence: dsliu@nfu.edu.tw; Tel.: +886-5-6315-665

Received: 24 November 2019; Accepted: 19 December 2019; Published: 21 December 2019



Abstract: In this study, pairs of the organosilicon/silicon oxynitride (SiO_xN_y) barrier structures with an ultralow water vapor transmittance rate (WVTR) were consecutively prepared by the plasma-enhanced chemical vapor deposition at a low temperature of 70 °C using the tetramethylsilane (TMS) monomer and the TMS-oxygen-ammonia gas mixture, respectively. The thickness of the SiO_xN_y film in the barrier structure was firstly designed by optimizing its effective permeability. The WVTR was further decreased by inserting an adequate thickness of the organosilicon layer as the stress residing in the barrier structure was released accordingly. By prolonging the diffusion pathway for water vapor permeation, three-paired organosilicon/ SiO_xN_y multilayered barrier structure with a WVTR of about 10^{-5} g/m²/day was achievable for meeting the requirement of the thin film encapsulation on the organic light emitting diode.

Keywords: organosilicon/silicon oxynitride barrier structure; water vapor transmittance rate; plasma-enhanced chemical vapor deposition; tetramethylsilane; thin film encapsulation

1. Introduction

Organic light emitting diodes (OLEDs) have become mainstream in the flat panel display developments because of their great advantage in efficiency, response time, viewing angle, and potential for flexible application. Unfortunately, the organic materials and the electrode metals in an unencapsulated OLED are easily be damaged by the permeation of water vapor, oxygen, and other contaminants present in ambient conditions, resulting in a serious reduction in device luminance [1–4]. To realize a long-living OLED device, a barrier coating to prevent water vapor and oxygen diffusion into the device structure is an important issue. Different from other optoelectronic devices, a barrier coating with an ultralow water vapor transmission rate (WVTR) below 10^{-4} g/m²/day is required for the organic solar cell and the OLED packaging [5,6]. To date, the conventional encapsulation method has been achieved by sealing the OLED device with a getter in an inert atmosphere using a rigid glass lid or metal, which causes the device to become more bulky and is incompatible with flexible application. Accordingly, thin and flexible barrier coatings with the high transmittance around visible

wavelengths, such as SiO_x , Si_3N_4 , and AlO_x , prepared by physical or chemical vapor deposition are potential candidates for thin film encapsulation (TFE) application [7–10]. However, the degree of the WVTR for these single barrier films [$\sim 10^0$ – 10^{-2} g/m²/day as it was coated onto the polyethylene terephthalate (PET) substrate] was orders-of-magnitude higher than the requirement for the TFE on the OLED (hereafter referred to as TFE-OLED) packaging. For realizing the TFE-OLED application, an organic/inorganic multilayered barrier structure with improvement on the inorganic structure and a longer pathway for the water vapor permeation is demonstrated to achieve an ultra-low WVTR ($<10^{-5}$ g/m²/day as it was coated onto the PET substrate) that approaches the requirement for the OLED packaging application [11,12]. To realize the deposition of an organic/inorganic multilayered structure, a process via switching the physical and/or the chemical vapor deposition, technologies including sputtering, atomic layer deposition, or plasma-enhanced chemical vapor deposition (PECVD) are commonly employed. Though the barrier performance of the organic/inorganic multilayered structure is theoretically qualified for the TFE-OLED application, the preparation of the structural organic and inorganic layers using at least two deposition systems/technologies is complicated, and the devices are prone to being contaminated. Thus, the organic/inorganic multilayered structure synthesized in a single-chamber deposition system employed by the chemical vapor deposition technology was developed [13,14].

In our previous work, we demonstrated a six-paired organosilicon/ SiO_x multilayered structure with a WVTR of about 10^{-5} g/m²/day, which was consecutively prepared by using one plasma-enhanced chemical vapor deposition system [15]. By optimizing the stress residing in the multilayered structure, a WVTR lower than 10^{-4} g/m²/day was obtained from the three-paired organosilicon/ SiO_x multilayered structure [16]. Moreover, the impact of the nitrogen atoms introduced into the SiO_x barrier film employed a PECVD system using the reactant gases of tetramethylsilane [TMS; $\text{Si}(\text{CH}_3)_4$, TMS], and oxygen with ammonia (NH_3) gas incorporation was also demonstrated [17]. The voids that appeared in the SiO_x film originating from the terminated bounds in the Si–O–Si networks were filled with the limited incorporation of nitrogen atoms as evidence of their surface morphologies, thus leading to improvement on the barrier performance. Under an adequate TMS–O₂–NH₃ gas mixture, the 100 nm thick silicon oxynitride (SiO_xN_y) film deposited onto the PET substrate performed more than one-order-of-magnitude reduction in the WVTR (0.06 g/m²/day) as compared to that of the SiO_x film (1.65 g/m²/day) synthesized from the TMS–O₂ gas mixture. However, though the barrier property of the SiO_x film to water vapor permeation was apparently improved as the nitrogen atoms were introduced into the Si–O–Si networks, the process temperature (120 °C) of this SiO_xN_y film and the above-mentioned organosilicon/ SiO_x multilayered structures were too high (120 °C) to employ as the TFE application on the organic-related devices, such as organic thin-film transistors (OTFTs), organic solar cells (OSCs), and organic light emitting diodes (OLEDs). Accordingly, low-temperature-deposited barrier films were essential to avoid thermal damage on these devices, which were composed of temperature-sensitive organic materials. In this work, with the aim to prepare the barrier film at a low temperature, the quality of the SiO_xN_y film as a function of the deposition temperature was firstly investigated. The thickness of the low temperature prepared SiO_xN_y film affected the resulting barrier property and was subsequently optimized. The barrier property of the SiO_xN_y film was deposited onto an organosilicon layer for optimizing the structural stress as well as the paired structures stacked from the organosilicon/ SiO_xN_y multilayered structure to greatly improve the resulting barrier performance, which was investigated and then followed by designing the thickness of the SiO_xN_y film. Eventually, the OLEDs encapsulated by these barrier structures were carried out to study the device's reliability and long-term stability.

2. Material Preparation and Experimental Procedure

SiO_xN_y barrier films were deposited onto cleaned silicon, PET, and polymethylmethacrylate (PMMA) substrates using a home-made planar-type capacitively coupled radio frequency (13.56 MHz) discharge PECVD system (hereafter referred to as TMS-PECVD). A vaporized source from liquid

TMS was employed as the silicon precursor and was mixed with the reactant gases of oxygen and ammonia. Detailed descriptions on the TMS reservoir and the design of the reactive chamber are reported elsewhere [7]. The gas flow rate of the TMS monomer was maintained at 60 sccm, and the gas flow ratios [$R = \text{NH}_3/(\text{O}_2 + \text{NH}_3)$] were controlled at 0.5 with a total gas flow rate ($\text{O}_2 + \text{NH}_3$) of 120 sccm. The TMS- O_2 - NH_3 gas mixture was dispersed through a shower head array. The deposition pressure and the radio frequency (RF) power were controlled at 27 Pa and 70 W, while the substrate temperature was controlled at ambient temperature ($\sim 30^\circ\text{C}$) and heated at 60, 70, 80, 90, 100, and 120°C , respectively, by a thermal heater system. To realize a quality barrier coating for TFE-OLED application at a low substrate temperature of 70°C , the barrier performance associated with the thickness of the SiO_xN_y films varied from 75 to 900 nm and was investigated. Following, paired organosilicon/ SiO_xN_y multilayered structures were consecutively deposited onto the above-mentioned substrates and the conventional OLEDs by this TMS-PECVD system using the tetramethylsilane (TMS) monomer and the TMS- O_2 - NH_3 gas mixture. The deposition pressure, the RF power, and the substrate temperature were fixed at 27 Pa, 70 W, and 70°C , respectively. The gas flow rate of the TMS monomer for synthesizing the organosilicon and the SiO_xN_y films was fixed at 60 sccm, and the gas flow rate ratio [$\text{NH}_3/(\text{O}_2 + \text{NH}_3)$] to react with the TMS for synthesizing the SiO_xN_y film was controlled at 0.5. The thickness of the SiO_xN_y film in the multilayered structure was fixed at 300 nm, while the thickness of the organosilicon layer was designed to optimize the structural residual stress.

Film thickness was measured using a surface profile instrument (Dektak 6M, Veeco, NY, USA) after averaging at least ten measurements and was confirmed by the cross-sectional investigations using the field emission scanning electron microscopy (FE-SEM; JSM-7500F, JEOL, Tokyo, Japan) observations. The dominated chemical bonds and the functional groups incorporation in the SiO_xN_y films as well as the atomic concentrations and the chemical bonding states on the films' surfaces while deposited at various substrate temperatures were examined using a Fourier transform infrared (FTIR) spectrometry (FT/IR-4100, JASCO, Easton, MD, USA) and an X-ray photoelectron (XPS) spectroscope (PHI Quantera SXMTM, ULVAC-PHI, Kanagawa, Japan). The pass energy for the XPS measurements was 20 eV with the energy scale of the spectrometer calibrated using the core level of Au $4f_{7/2}$ at 83.9 eV. Surface and cross-sectional morphologies of the single SiO_xN_y film and pairs of the multilayered structures were observed by the FE-SEM instrument operated at 15 kV. The internal stress, σ_f , resided in the barrier structures while they were deposited onto the PMMA substrates and was derived from the Stoney formula, expressed as [18]:

$$\sigma_f = \frac{E_s d_s^2}{6(1 - \nu_s) d_f} \left(\frac{1}{R_f} - \frac{1}{R_0} \right) \quad (1)$$

where E_s , ν_s , and d_s are the constants of Young's modulus, Poisson ratio, and thickness of the substrate, which were 0.25 GPa, 0.39, and 1.6 mm. d_f is the total thickness of the barrier structures. R_0 and R_f are the radii of the sample curvatures before and after depositing, which were conducted to form the surface profile instrument (Dektak 6M) measurements. The water vapor permeation of these barrier structures encapsulated onto the PET substrates was measured using a WVTR measurement system (MOCON Inc., PERMATRAN-W3/61, Minneapolis, MN, USA) at a temperature of 40°C with 95% relative humidity (RH). For the structures that performed the barrier property below the MOCON test limitation (i.e., WVTR < 10^{-3} g/m²/day), a calcium (Ca) degradation test under the atmospheric environment was conducted to evaluate their WVTRs by observing the percentage of the hydrolyzation (corrosion) area in which the color was changed within dimensions of 15 mm \times 15 mm using an optical microscope. In addition, the current density–voltage (J – V) and luminance–voltage (L – V) properties of the OLEDs with and without the thin film encapsulation were measured using a semiconductor parameter analyzer and an integrated sphere detector.

3. Results and Discussions

Figure 1 shows the deposition rates of the SiO_xN_y film as a function of the substrate temperature. The deposition rate of the SiO_xN_y films synthesized from the glow discharge of the TMS- O_2 - NH_3 gas

mixture at ambient temperature (~ 15.6 nm/min) was significantly decreased to about 13.5 nm/min at the substrate temperature of 60 °C, and then it was gradually saturated to about 12.5 nm/min as the substrate temperature reached 120 °C. One of the reasons for the reduction in the deposition rate with the deposition temperature increasing was ascribed to the enhancement in the lateral diffusion of the products on the coating surface at an elevated temperature. Meanwhile, the evolutions of the physic- to chemi-adsorptions on the surface that were activated by the substrate temperature were likely to be the main reason for the sharp decrease in the deposition rate as the temperature increased from 30 to 60 °C, which may have resulted in the film densification and a better adhesion to the substrate. The chemical bond configurations of the 100 nm-thick SiO_xN_y films as a function of the substrate temperature conducted from the FTIR spectra are illustrated in Figure 2a. All these spectra show a dominated Si–O–Si stretching mode at around 1062 cm^{-1} with a tail extending to higher wavenumbers. A weak peak located at 794 cm^{-1} emerged from the Si–O–Si bending mode, and a broad band around $2800\text{--}3700\text{ cm}^{-1}$ was denoted as the hydroxyl (–OH) chemical bonds. Figure 2b depicts a high-resolution image of the wavenumbers, which ranged from 900 to 1300 cm^{-1} for the samples deposited at 30, 70, and 120 °C, respectively. The spectra were composed of a significant Si–O–Si stretching mode (denoted as TO_3 in Figure 2b) and a shoulder that could be deconvoluted into three peaks at about 1101, 1143, and 1194 cm^{-1} , respectively. As referred to in the reports [15,17,19–21], these peaks could be identified as the C–H/C–C bonds and the second asymmetric modes of the longitudinal-optic (LO_4) and the transverse-optic (TO_4) vibration pairs in the Si–O–Si networks. The formation of the C–H/C–C bond was ascribed to the plasma polymerization of only the TMS monomer, whereas the intensity of the TO_4 mode corresponded to the degree of the structural disorder in the Si–O–Si networks. Compared to the SiO_xN_y films deposited onto the heated substrate (70 and 120 °C), a significant C–H/C–C bond synthesized from the TMS polymerization appeared in the film deposited onto the substrate under ambient temperature (30 °C). In addition, the relative intensity of the Si–O–Si stretching bonds (TO_3) to the C–H/C–C bond and to the TO_4 mode in the SiO_xN_y film deposited at 120 °C was increased as compared to the film prepared at a substrate temperature of 70 °C. The low relative intensity of the C–H/C–C bond obtained from the 120 °C-deposited SiO_xN_y film revealed that the chemical reaction in glow discharge from the TMS- O_2 - NH_3 gas mixture to form the Si–O chemical bond was more effective at an elevated temperature. Meanwhile, this deposition temperature was also beneficial for suppressing the intensity of the signal of the TO_4 mode, indicating better film densification with the ordered Si–O–Si networks.

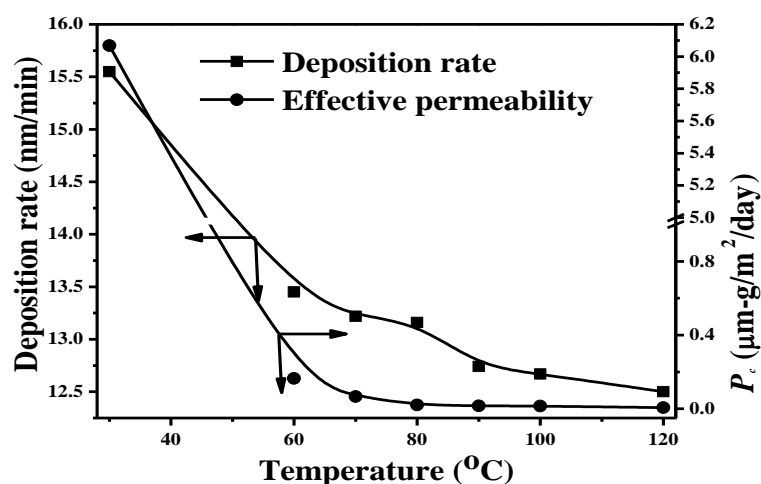


Figure 1. Deposition rates and effective permeability of the SiO_xN_y film as a function of the substrate temperature.

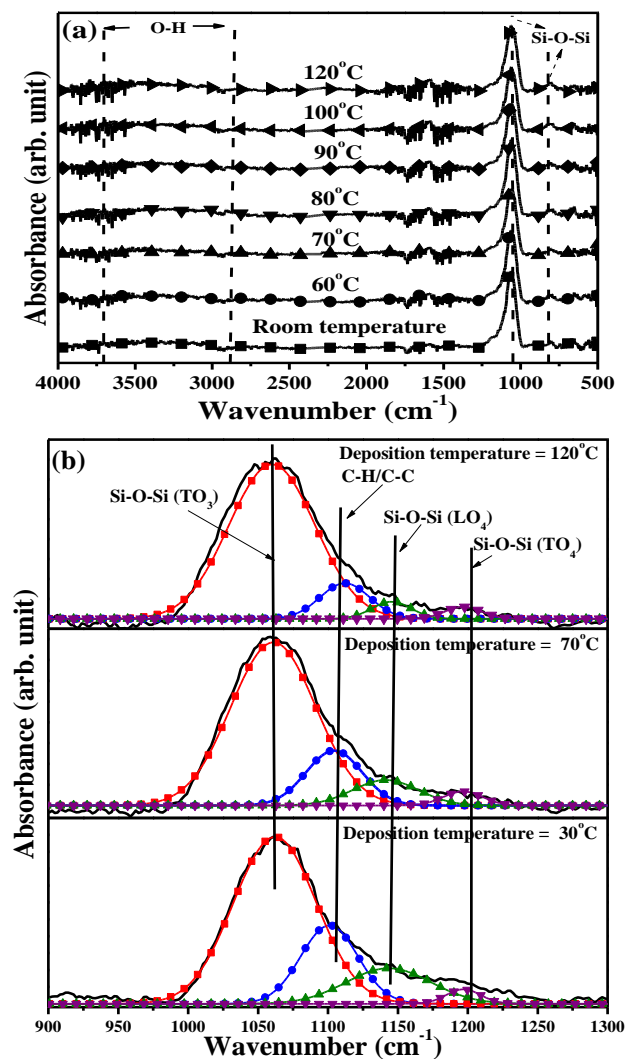


Figure 2. (a) Chemical bond configurations of the 100 nm-thick SiO_xN_y films as a function of the substrate temperature and (b) high-resolution of the wavenumbers ranged from 900 to 1300 cm^{-1} for the samples deposited at 30, 70, and 120 °C, respectively.

The XPS survey spectra for the SiO_xN_y films deposited at the substrate temperatures of 70 and 120 °C are displayed in Figure 3a. These spectra showed main peaks of Si 2p and O 1s centered at the binding energies of 104 and 533 eV, respectively. Two weak peaks denoted as C 1s and N 1s could be seen at 285 and 399 eV. Figure 3b gives the changes in the atomic concentration of the synthesized SiO_xN_y films as a function of the substrate temperatures (the evolution of the N/C atomic ratio on the SiO_xN_y film surface was also calculated). The atomic concentrations of the elements Si and O for the SiO_xN_y film deposited at room temperature were about 33.2% and 63.8%, respectively, to result in an atomic ratio of about 1.92. The atomic ratio (O/Si) was gradually increased with the deposition temperature increasing and was saturated to about 1.98 as the substrate temperature reached 70 °C. Moreover, though the atomic concentration of the elemental nitrogen introduced into the films was limited in the range of 1.12 at.%–1.38 at.%, the atomic ratio of N/C for the samples deposited at a temperature of 70 °C was markedly increased from 0.77 to 1.84 as the SiO_xN_y film synthesized at 120 °C. This showed evidence of the deposition temperature being beneficial for the introduction of the nitrogen atoms and also for the decomposition of TMS precursor to cause a decrease in the carbon atoms in the synthesized films. Figure 4a–d highlights the narrow scan of Si 2p, O 1s, N 1s, and C 1s core levels for the SiO_xN_y films deposited at the substrate temperatures of 70 and 120 °C. In Figure 4a, the peak of the Si 2p core level for the SiO_xN_y films deposited at 70 °C was located at 103.8 eV,

while that of the film deposited at 120 °C shifted to 103.5 eV, which corresponded well to the Si–O–Si chemical bond in the SiO_x matrix [22,23]. The shift of the Si 2*p* peak toward a higher binding energy for the SiO_xN_y films deposited at 70 °C was attributed to the signal that emerged from the Si atoms, which was surrounded by the undissociated oxygen molecule (i.e., oxygen-rich condition) [24,25]. Moreover, the additive area at the lower binding energy for the SiO_xN_y films deposited at 120 °C could be ascribed to the existence of the N–Si–O bond originating from the nitrogen atom in substitution for the oxygen atom in the O–Si–O networks, since the peak of the Si₃N₄ was known to be in the low binding energy of 101.6–102.1 eV [26–28]. The O 1*s* core level, as shown in Figure 4b, of the SiO_xN_y films deposited at 120 °C had a peak at 532.8 eV, whereas that of the film deposited at 70 °C was at 533 eV. Considering the composition of the SiO_xN_y film and that referred to in the reports [22,29–32], this peak was composed of at least three main chemical bonds, which in turn were assigned to the unbounded oxygen (O⁺), the oxygen bonded to silicon (Si–O), and the nitrogen/carbon ions bonded to oxygen (N–O/C–O) with chemical states at about 533.8, 532.9, and 531.5 eV, respectively. The shift of the peak toward a high binding energy for the film deposited at 70 °C could be ascribed to more unbounded oxygen ions in the O–Si–O networks, while the prominent part at a low binding energy for the film deposited at 120 °C could be ascribed to the nitrogen atoms incorporating the Si–O matrix to form the N–O chemical bond state. The binding energy of the N 1*s* core level for both coatings, shown in Figure 4c, appeared as a peak at about 398.7 eV, a value higher than the Si–N bond in the Si₃N₄ film (~397.4 eV) [26,27,33]. This shift of the binding energy confirmed the existence of the Si–O–N chemical bond (~398.2–399.6 eV), as referred to in the reports on the plasma polymerized SiO_xC_yN_z, the oxygen plasma modified Si₃N₄ films, and the annealed SiON ceramic [23,26,28,34]. Another weak peak at approximately at 400.9 eV, measured only from the 70 °C-deposited SiO_xN_y film, was assigned to the N–H bond originating from the incomplete decomposition of the protonation of the amine group [35]. By contrast, the difference in the C 1*s* spectra between the SiO_xN_y films deposition at 70 and 120 °C, shown in Figure 4d, was insignificant. Both of these curves contained a main peak at 284.6 eV, which corresponded to the sp²-hybridized carbon atom (C–H/C–C) states with a shoulder related to the Si–O–C bond (285.6 eV) extending to high binding energy, and a weak signal ranged from 288.5–291.5 eV and was associated with the carbon oxygenated (C–O/C=O) groups [22,30,35,36]. The above investigations of the XPS measurements on the synthesized SiO_xN_y films showed evidence that the deposited temperature was beneficial for the introduction of the nitrogen atoms into the SiO_x-based film, while the carbon atoms were decreased concurrently. Those nitrogen atoms introduced into the Si–O–Si matrix at an elevated substrate temperature were prone to form the nitrogen-related chemical states as a substitution for the lattice silicon and the oxygen ions and thus were responsible for the densification of the SiO_xN_y film due to its smaller ionic radius compared to the oxygen ion.

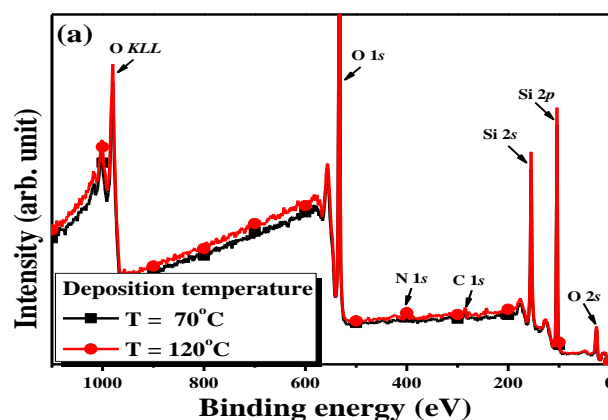


Figure 3. Cont.

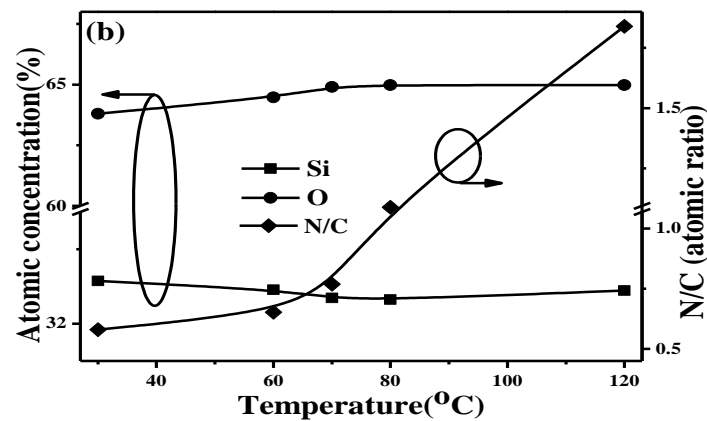


Figure 3. (a) X-ray photoelectron spectroscopy (XPS) survey spectra for the SiO_xN_y films deposited at the substrate temperatures of 70 and 120 °C, respectively, and (b) changes in the atomic concentration and the N/C atomic ratio as a function of the substrate temperatures.

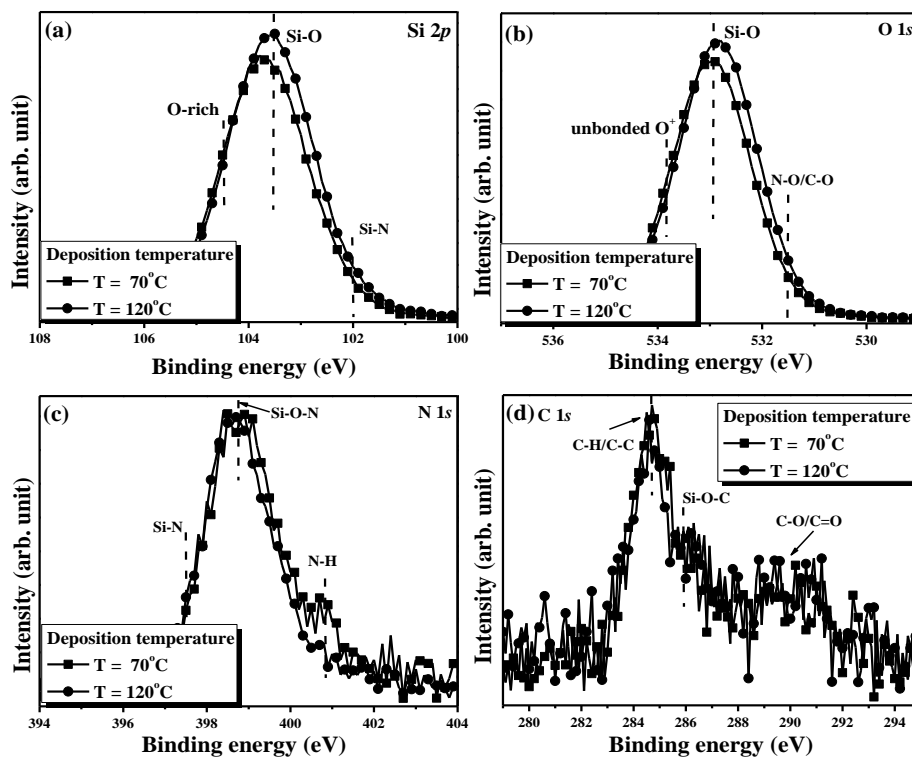


Figure 4. Narrow scan of (a) Si 2p, (b) O 1s, (c) N 1s, and (d) C 1s core levels for the SiO_xN_y films deposited at the substrate temperatures of 70 and 120 °C.

The WVTR and the effective permeability of the 100 nm-thick SiO_xN_y films synthesized at various temperatures when deposited onto the PET substrates are summarized in Table 1. The effective permeability, P_c , to evaluate the coating quality with the effect of the PET substrate eliminated, as listed in Table 1, was derived from the following equation using ideal laminate theory (ILT) [37]:

$$\frac{1}{\Pi_T} = \frac{d_T}{P_T} = \frac{d_s}{P_s} + \frac{d_c}{P_c} \quad (2)$$

where Π is the transmission rate, P is permeability, and d is thickness; the subscripts s , c , and T denote the substrate, the barrier coating, and the combination structure ($s + c$), respectively. The evolution of the effective permeability on the SiO_xN_y film as a function of the deposition temperature is

plotted in Figure 1. The barrier property to the water vapor permeation for the PET substrate showed little improvement after coating with the SiO_xN_y film prepared under ambient temperature. The 60 °C-deposited SiO_xN_y film coated onto the PET substrate resulted in a marked decrease in the WVTR ($\sim 1.13 \text{ g/m}^2/\text{day}$). Moreover, compared to the related concentration of the nitrogen atoms on the SiO_xN_y film surface (Figure 3b), the evolution of the effective permeability, as shown in Figure 1, implied the quality of the film as a barrier for water vapor permeation and was found to be well correlated with the increase in the nitrogen atoms incorporated into the SiO_xN_y film. Accordingly, the PET substrate encapsulated by the 120 °C-deposited SiO_xN_y film, which had a high related concentration of nitrogen ions (atomic ratio of N/C ~ 1.84) to form the dense Si–O–N/Si–N chemical bonds, performed two-orders-of-magnitude in the WVTR ($\sim 6 \times 10^{-2} \text{ g/m}^2/\text{day}$) lower than the bare PET substrate. The current density–voltage and luminance–voltage curves for the TFE-OLED packaging using the 120 °C- and the 70 °C-deposited SiO_xN_y films, respectively, are illustrated in Figure 5a,b, respectively (the OLED encapsulated by the conventional glass lid is given for comparison). Compared to the commercial OLED device packaged by the glass lid, the device performance was almost unchanged as it was directly encapsulated by the 70 °C-deposited SiO_xN_y film, whereas an apparent degradation in the forward current was measured from the 120 °C-deposited SiO_xN_y film packaged OLED device. A marked decrease in the luminance, as can be seen in Figure 5b, was also measured from the 120 °C- SiO_xN_y film encapsulated OLED device. By contrast, the resulting luminance of the OLED device encapsulated by the 70 °C- SiO_xN_y film was shown to be a little higher ($\sim 8\%$) than the glass lid packaged OLED device at a bias voltage of 8 V, which could have been attributed to the barrier film also being beneficial for the passivation of the surface non-radiation centers. Consequently, though the 120 °C-deposited SiO_xN_y film showed a barrier property superior to the film deposited at 70 °C, the deposition temperature to prepare this barrier film was too high to apply as a TFE for OLED device packaging. In contrast, the SiO_xN_y film synthesized at a low temperature of 70 °C was harmless to the device performance and was a promising candidate for the TFE-OLED device application. Unfortunately, the barrier property of the 70 °C-deposited SiO_xN_y film was orders-of-magnitude higher than the requirement for the application to OLED device packaging. Thus, methodology to optimize the barrier property to the water vapor permeation of the 70 °C-deposited SiO_xN_y film for TFE-OLED application was essential.

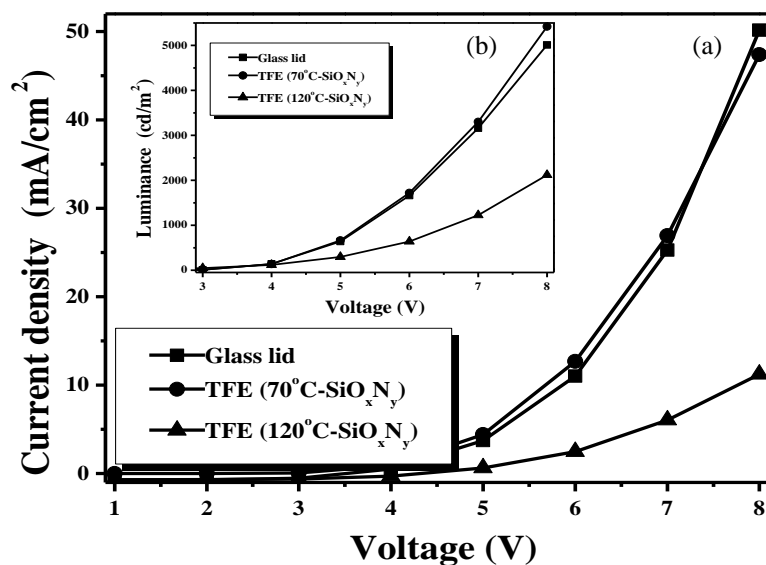


Figure 5. (a) Current density–voltage and (b) luminance–voltage for the thin film encapsulation (TFE)-organic light emitting diodes (OLED) packaging using the 120 °C- and the 70 °C-deposited SiO_xN_y film, respectively (the OLED encapsulated by the conventional glass lid is given for comparison).

Table 1. Barrier performance of the 100 nm-thick SiO_xN_y films synthesized at various temperatures when deposited onto the polyethylene terephthalate (PET) substrates (measurements taken at 40 °C with 95% relative humidity (RH)).

Substrate Temperature (°C)	30	60	70	80	90	100	120
WVTR (g/m ² /day)	3.40	1.13	0.56	0.19	0.16	0.14	0.06
P_c ($\mu\text{m-g/m}^2/\text{day}$)	6.068	0.165	0.066	0.021	0.016	0.015	0.006

The water vapor transmittance rate (WVTR) of the bare PET is 3.61 g/m²/day.

In order to optimize the barrier property of the 70 °C-deposited SiO_xN_y film, the thickness of the SiO_xN_y film, which was beneficial to prolonging the diffusion length of the water vapor permeation, was firstly designed. The barrier performance of the 70 °C-deposited SiO_xN_y film, which was deposited onto the PET substrate as a function of the film thickness, is listed in Table 2. The evolutions of the WVTR and the effective permeability are highlighted in Figure 6. As the PET substrate was coated with a 75 nm-thick SiO_xN_y film, the WVTR was markedly decreased from 3.61 to 0.83 g/m²/day. The WVTR of the PET substrates coated with the SiO_xN_y film was gradually decreased as the film thickness increased, and the lowest value of 0.20 g/m²/day was obtained from the 300 nm-thick SiO_xN_y film deposited onto the PET substrate. However, as the film thickness reached 400 nm, which should have corresponded to a longer diffusion length for the water vapor transmission than the thickness of 300 nm, the resulting WVTR was increased to 0.28 g/m²/day. The reason for the degradation of the barrier property was ascribed to less structural order and film densification due to the appearance of pinholes, micro-pores, and micro-cracks in the SiO_xN_y film [15,38,39]. The WVTR of the PET substrate was then degraded to 0.98 g/m²/day as it was coated with a 900 nm-thick SiO_xN_y film. The evolution of the effective permeability shown in Figure 6 also showed sharp degradation of film quality starting as the thickness of the SiO_xN_y film reached 400 nm. To realize a long diffusion path for water vapor permeation in the SiO_xN_y film without structural degradation, pairs of organosilicon/ SiO_xN_y multilayered barrier structures with optimized residual internal stress, as quoted from our previous report [15,16], were engineered.

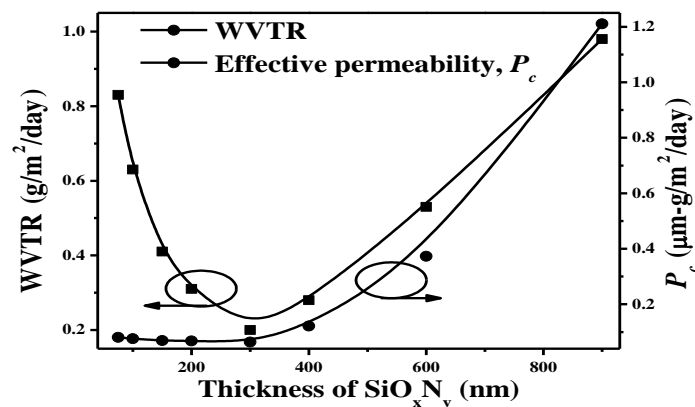


Figure 6. Evolutions of the WVTR and the effective permeability of the 70 °C-deposited SiO_xN_y film, which was deposited onto the PET substrate as a function of the film thickness.

Table 2. Barrier performance of the 70 °C-prepared SiO_xN_y films as a function of the films' thicknesses when deposited onto the PET substrates (measurements taken at 40 °C with 95% RH).

Film Thickness (nm)	75	100	150	200	300	400	600	900
WVTR (g/m ² /day)	0.83	0.63	0.41	0.31	0.20	0.28	0.53	0.98
P_c ($\mu\text{m-g/m}^2/\text{day}$)	0.068	0.066	0.077	0.070	0.063	0.121	0.372	1.211

Figure 7 plots the evolution of the WVTR and the residual internal stress as a function of the thickness of the organosilicon buffer layer inserted between the 300 nm-thick SiO_xN_y film and the

substrate. The barrier property of the SiO_xN_y film was improved as it was deposited onto the organosilicon buffer layer, while the structural internal compressive stress was decreased. A reduction of 40% in the WVTR was achieved from the SiO_xN_y film deposited onto a 30 nm-thick organosilicon (from 0.20 to 0.12 $\text{g}/\text{m}^2/\text{day}$). Meanwhile, this one-paired organosilicon/ SiO_xN_y multilayered structure coated onto the PMMA substrate also corresponded to the lowest internal compressive stress of about 61 MPa. It showed evidence of the internal compressive stress as the SiO_xN_y film directly deposited onto the PMMA substrate (~ 78 MPa), which might have induced the structural cracks that could be adequately buffered as the organosilicon layer was introduced, thereby further enhancing the film's barrier property to water vapor permeation. However, as the thickness of the organosilicon layer was higher than 30 nm, an increase in the residual compressive stress of the one-paired organosilicon/ SiO_xN_y multilayered structure was measured, and thus the resulting barrier property was degraded. Based on this methodology, a two-paired organosilicon/ SiO_xN_y multilayered structure with the optimal internal residual stress set as the thickness of the second organosilicon layer of 60 nm was designed. The resulting WVTR of this two-paired organosilicon/ SiO_xN_y multilayered structure consecutively deposited onto the PET substrate was markedly decreased to 0.06 $\text{g}/\text{m}^2/\text{day}$. Moreover, the stress controlled three-paired organosilicon/ SiO_xN_y structure with the third organosilicon layer of 60 nm deposited onto the PET substrate resulted in a WVTR below the detection limit (<0.01 $\text{g}/\text{m}^2/\text{day}$) of the MOCON Permatran-W3/61. The surface morphologies of the 300 nm-thick SiO_xN_y film, the one-paired, and the three-paired organosilicon/ SiO_xN_y multilayered structures are shown in Figure 8a–c, respectively (the corresponding cross-sectional morphologies are given in Figure 8a1–c1). In Figure 8a, significant white protrusions in circular shapes (as indicated by arrows) associated with the coverage of the voids were distributed over the surface of the SiO_xN_y film [17,40,41]. Cracks from the substrate to the film surface could be seen in Figure 8a1. By contrast, no protrusions were observed from the surface of the SiO_xN_y film deposited onto an organosilicon buffer layer (Figure 8b). Meanwhile, cracks were almost absent from Figure 8b1. This showed evidence that the organosilicon coating onto the substrate prior to the SiO_xN_y deposition facilitated not only the improvement in the resulting surface roughness and densification but also the suppression of the crack growth, thereby increasing the barrier property of the SiO_xN_y film to water vapor permeation. The surface uniformity and densification were further improved, as observed from the particles distributed over the surface of the three-paired organosilicon/ SiO_xN_y multilayered structure (Figure 8c), and became more ambiguous and smaller when compared to those that appeared in Figure 8b. Each of the organosilicon interlayers and the SiO_xN_y films without cracks growth could be clearly identified from the inset cross-sectional image (Figure 8c1). Such a thick and dense SiO_xN_y film without cracks constructed from the three-paired organosilicon/ SiO_xN_y multilayered structure confirmed a longer pathway for the water vapor permeation and thereby resulted in a structure with an ultra-low WVTR.

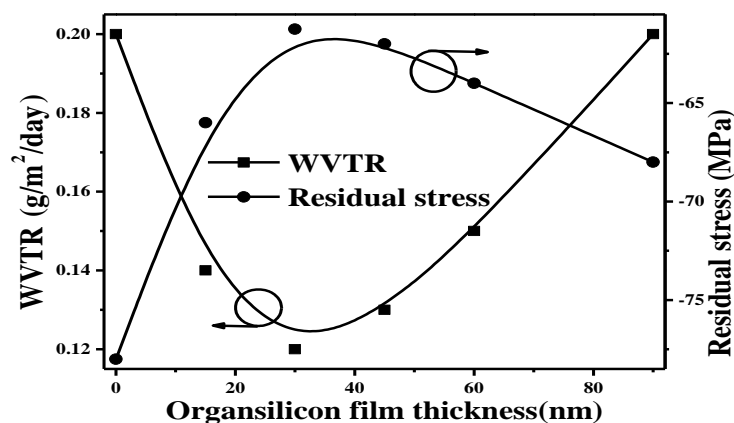


Figure 7. Evolution of the WVTR and the residual internal stress as a function of the thickness of the organosilicon buffer layer inserted between the 300 nm-thick SiO_xN_y film and the substrate.

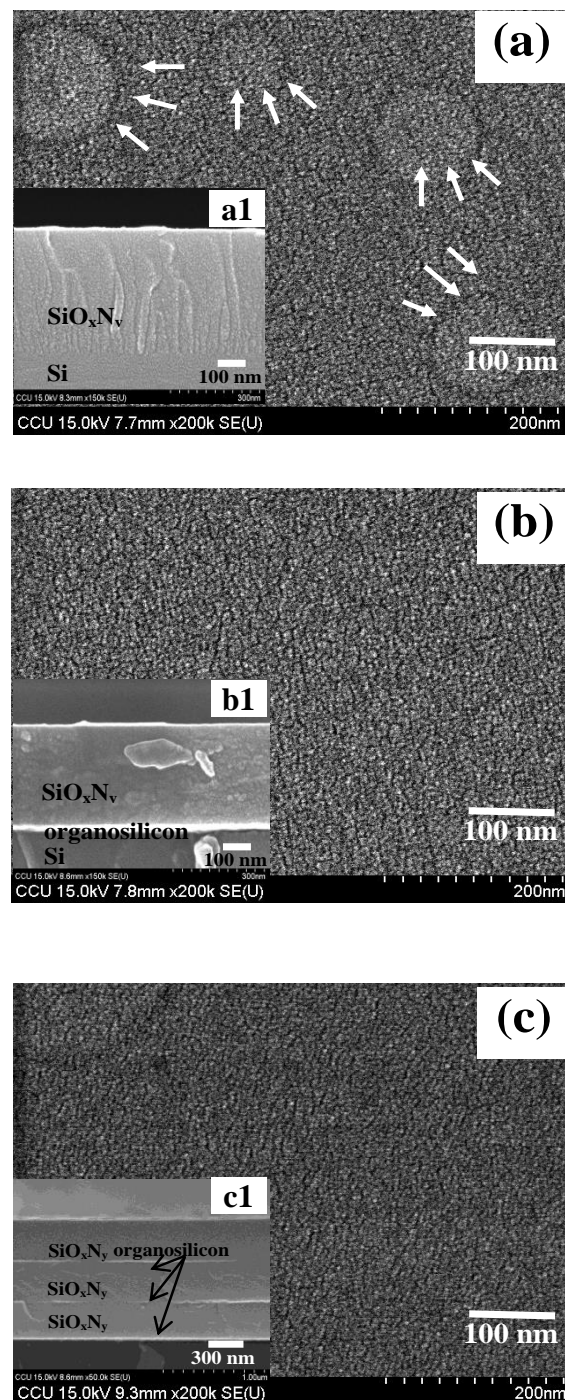


Figure 8. Surface morphologies of the (a) 300 nm-thick SiO_xN_y film, (b) 1-paired, and (c) 3-paired organosilicon/ SiO_xN_y multilayered structures, respectively (the corresponded cross-sectional morphologies also are given in the inset figures: (a1) 300 nm-thick SiO_xN_y film, (b1) 1-paired, and (c1) 3-paired organosilicon/ SiO_xN_y structures).

For the WVTR of the three-paired organosilicon/ SiO_xN_y multilayered structure deposited onto the PET substrate below the detection limit of the MOCON Permatran-W3/61, it was evaluated through the percentage of the corrosion area observed from the images of the Ca test. Figure 9 shows the corrosion area as a function of aging time under the atmospheric environment (the Ca test images as the sample aged at 5, 10, 20, and 30 days are also shown in the inset figures). The corrosion area of the Ca test was linearly proportional to the aging time. The percentage of the corrosion area for the sample aged

at 5 days was about 0.052%, and there was only a slight increase (~0.816%) in the corrosion area as the aging time reached 30 days. The corresponding WVTR was evaluated from each change of the corrosion area using the following equation [42]:

$$\text{WVTR} = 2d \left(\frac{M_{\text{H}_2\text{O}}}{M_{\text{Ca}(\text{OH})_2}} \right) \rho_{\text{Ca}(\text{OH})_2} \left[\frac{dS}{dt} \right] \left(\frac{1}{S_{\text{Ca}}} \right) \quad (3)$$

where d and S_{Ca} are the thickness and the area of the calcium film; $M_{\text{H}_2\text{O}}$ and $M_{\text{Ca}(\text{OH})_2}$ are the molecular weight (g/mole) of water and calcium hydroxide; $\rho_{\text{Ca}(\text{OH})_2}$ is the density of calcium hydroxide (g/m³), and $\frac{dS}{dt}$ is the rate of change in the percentage of the corrosion area (m²/day).

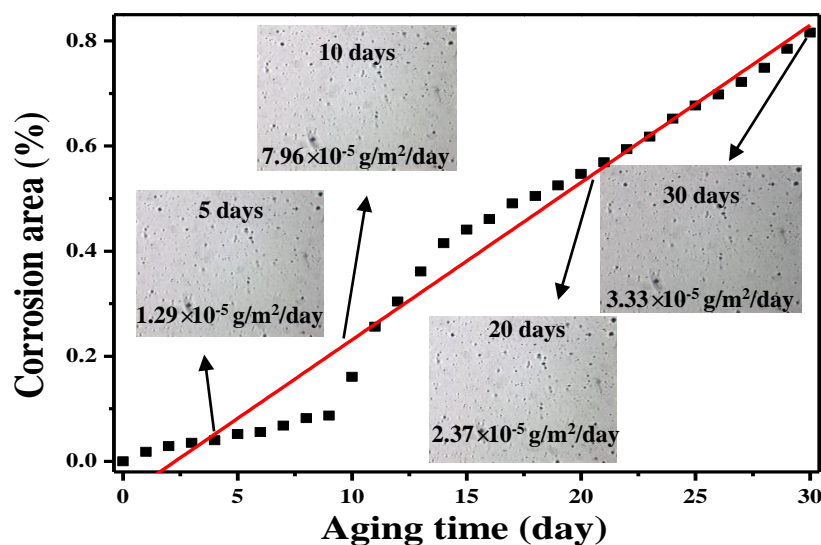


Figure 9. Corrosion area as a function of aging time under the atmospheric environment (the Ca test images as the sample aged at 5, 10, 20, and 30 days are also shown in the inset figures).

The WVTR calculated from Figure 9 ranged from 1.02×10^{-4} to 4.30×10^{-6} g/m²/day, a value that met the requirement for the TFE-OLED application. The subsequent evolutions of the electroluminescence (EL) to the initial EL intensity ($L_0 = 300$ cd/m²), L/L_0 , from the green OLEDs directly encapsulated by a single 300 nm-thick SiO_xN_y film and the three-paired organosilicon/ SiO_xN_y multilayered structure are depicted in Figure 10 [the evolution of the OLED without TFE encapsulation (i.e., bare OLED) is given as a comparison]. The EL intensity of the bare OLED decreased sharply as the operation time increased. The time, T_{50} defined as the EL intensity decreased to half of the initial intensity ($L/L_0 = 0.50$) and was lower than 50 h (~44 h). By contrast, the reduction in the EL intensity became less abrupt as a 300 nm-thick SiO_xN_y film encapsulated onto the OLED device, and the T_{50} was apparently increased to 295 h. When the device was encapsulated by the three-paired organosilicon/ SiO_xN_y multilayered structure, which showed an excellent barrier property to water vapor permeation, the EL intensity was almost unchanged, even as the device was operated for a time longer than 300 h ($L/L_0 \sim 0.98$). Such a stable OLED confirmed the feasibility of this low temperature deposited three-paired organosilicon/ SiO_xN_y multilayered structure, which was consecutively synthesized using the TMS-PECVD system for the TFE application.

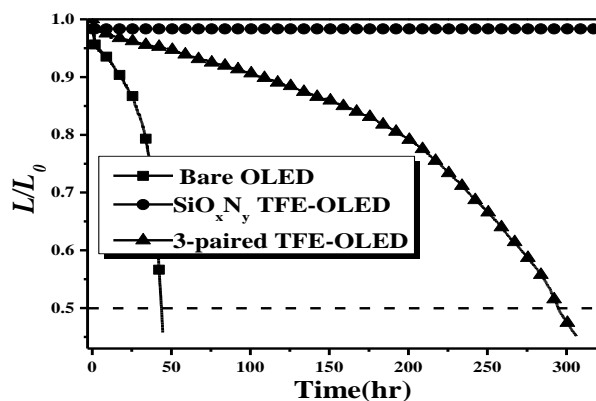


Figure 10. Evolution of the electroluminescence (L) to the initial EL intensity for the OLEDs directly encapsulated by the 300 nm-thick SiO_xN_y film and the three-paired organosilicon/ SiO_xN_y multilayered structure [evolution of the OLED without TFE encapsulation (i.e., bare OLED) is given as a comparison].

4. Conclusions

In summary, a paired organosilicon/ SiO_xN_y multilayered structure with an ultra-high barrier quality for the TFE-OLED application was realized by consecutively using the TMS-PECVD system at a low temperature. The deposited temperature and thickness of the SiO_xN_y film in the multilayered structure were firstly designed at 70 °C and 300 nm, respectively, to perform an optimized effective permeability of about 0.063 ($\mu\text{m}\cdot\text{g}/\text{m}^2/\text{day}$) without damaging the OLED performance. The quality and the densification of the low temperature prepared SiO_xN_y film were then improved as an adequate organosilicon buffer layer was inset before the SiO_xN_y film deposition originating from the release of the structural residual stress. The resulting WVTR of the 300 nm-thick SiO_xN_y film was further decreased from 0.20 to 0.12 $\text{g}/\text{m}^2/\text{day}$ as it was deposited onto a 30 nm-thick organosilicon buffer layer, which also corresponded to a low residual compressive stress of 61 MPa. By this methodology, an ultra-low WVTR ($\sim 10^{-5}$ $\text{g}/\text{m}^2/\text{day}$) evaluated by the Ca test was achieved from the three-paired organosilicon/ SiO_xN_y multilayered structure consecutively deposited onto the PET substrate. The reliability and the stability of the OLED device was greatly improved as it was directly encapsulated by this three-paired organosilicon/ SiO_xN_y multilayered structure, which was prepared at a low temperature of 70 °C using one TMS-PECVD system.

Author Contributions: Organization, conceptualization, and methodology procedures, D.-S.L.; measurement apparatus support and paper preparation, M.-Y.C. and T.-H.C.; film deposition and device fabrication, R.-D.F. and C.K.C.; data curation and investigation, S.-K.L. All authors have read and agreed to the published version of the manuscript.

Funding: This research received no external funding.

Acknowledgments: The authors would like to thank the support of Ministry of Science and Technology under MOST 108-2622-E-150-012-CC3 and the fund supports by ITRI and MIRDC.

Conflicts of Interest: The authors declare no conflict of interest.

References

1. Aziz, H.; Popovic, Z.; Tripp, C.P.; Hu, N.X.; Hor, A.; Xu, G. Degradation processes at the cathode/organic interface in organic light emitting devices with Mg:Ag cathodes. *Appl. Phys. Lett.* **1998**, *72*, 2642–2644. [[CrossRef](#)]
2. Lien, K.K.; Chua, S.J.; Lim, S.F. Influence of electrical stress voltage on cathode degradation of organic light-emitting devices. *J. Appl. Phys.* **2001**, *90*, 976–979. [[CrossRef](#)]
3. Liew, Y.F.; Aziz, H.; Hu, N.X.; Chan, H.S.O.; Xu, G.; Popovic, Z. Investigation of the sites of dark spots in organic light-emitting devices. *Appl. Phys. Lett.* **2000**, *77*, 2650–2652. [[CrossRef](#)]

4. Burrows, P.E.; Graff, G.L.; Gross, M.E.; Martin, P.M.; Hall, M.; Mast, E.; Bonham, C.; Bennett, W.; Michalski, L.; Weaver, M.; et al. Gas permeation and lifetime tests on polymer-based barrier coatings. *Proc. SPIE* **2001**, *4105*, 75.
5. Chen, T.N.; Wu, D.S.; Wu, C.C.; Chiang, C.C.; Chen, Y.P.; Horng, R.H. High performance transparent barrier films of SiO_x/SiN_x stacks on flexible substrates. *J. Electrochem. Soc.* **2006**, *153*, 244–248. [[CrossRef](#)]
6. Cros, S.; de Bettignies, R.; Berson, S.; Bailly, S.; Maise, P.; Lemaitre, N.; Guillere, S. Definition of encapsulation barrier requirements: A method applied to organic solar cells. *Sol. Energy Mater. Sol. Cells* **2011**, *95*, S65–S69. [[CrossRef](#)]
7. Wu, C.Y.; Chen, W.C.; Liu, D.S. Surface modification on flexible substrates by plasma-enhanced chemical vapor deposition using tetramethylsilane-oxygen gas mixture. *J. Phys. D Appl. Phys.* **2008**, *41*, 225305. [[CrossRef](#)]
8. Lee, G.H.; Yun, J.; Lee, S.; Jeong, Y.; Jung, J.H.; Cho, S.H. Investigation of brittle failure in transparent conductive oxide and permeation barrier oxide multilayers on flexible polymers. *Thin Solid Films* **2010**, *518*, 3075–3080. [[CrossRef](#)]
9. Saleem, M.R.; Ali, R.; Honkanen, S.; Turunen, J. Thermal properties of thin Al₂O₃ films and their barrier layer effect on thermo-optic properties of TiO₂ films grown by atomic layer deposition. *Thin Solid Films* **2013**, *542*, 257–262. [[CrossRef](#)]
10. García-Valenzuela, A.; López-Santos, C.; Rico, V.; Alvarez, R.; Palmero, A.; González-Elipe, A.R. Environmentally tight TiO₂-SiO₂ porous 1D-Photonic structures. *Adv. Mater. Interfaces* **2018**, *6*, 1801212. [[CrossRef](#)]
11. Graff, G.L.; Williford, R.E.; Burrows, P.E. Mechanisms of vapor permeation through multilayer barrier films: Lag time versus equilibrium permeation. *J. Appl. Phys.* **2004**, *96*, 1840–1849. [[CrossRef](#)]
12. Fahlteich, J.; Fahland, M.; Schonberger, W.; Schiller, N. Permeation barrier properties of thin oxide films on flexible polymer substrates. *Thin Solid Films* **2009**, *517*, 3075–3080. [[CrossRef](#)]
13. Kim, T.W.; Yan, M.; Erlat, A.G.; Mcconnelee, P.A.; Pellow, M.; Deluca, J.; Feist, T.P.; Duggal, A.R.; Schaepkens, M. Transparent hybrid inorganic/organic barrier coatings for plastic organic light-emitting diode substrates. *J. Vac. Sci. Technol. A* **2005**, *23*, 971–977. [[CrossRef](#)]
14. Patelli, A.; Vezzu, S.; Zottarel, L.; Menin, E.; Sada, C.; Martucci, A.; Costacurta, S. SiO_x-based multilayer barrier coatings produced by a single PECVD process. *Plasma Process. Polym.* **2009**, *6*, S665–S670. [[CrossRef](#)]
15. Wu, C.Y.; Liao, R.M.; Lai, L.W.; Jeng, M.S.; Liu, D.S. Organosilicon/silicon oxide gas barrier structure encapsulated flexible plastic substrate by using plasma-enhanced chemical vapor deposition. *Surf. Coat. Technol.* **2012**, *206*, 4685–4691. [[CrossRef](#)]
16. Lu, S.K.; Chen, S.C.; Chen, T.H.; Lai, L.W.; Liao, R.M.; Liu, D.S. Barrier property and mechanical flexibility of stress controlled organosilicon/silicon oxide coatings on plastic substrates. *Surf. Coat. Technol.* **2015**, *280*, 92–99. [[CrossRef](#)]
17. Liu, H.W.; Chen, T.H.; Chang, C.H.; Lu, S.K.; Lin, Y.C.; Liu, D.S. Impact on the gas barrier property of silicon oxide films prepared by tetramethylsilane-based PECVD incorporating with ammonia. *Appl. Sci.* **2017**, *7*, 56. [[CrossRef](#)]
18. Bhatt, V.; Chandra, S.; Kumar, S. Stress evaluation of RF sputtered silicon dioxide films for MEMS. *Indian J. Pure Appl. Phys.* **2007**, *45*, 377–381.
19. Kirk, C.T. Quantitative analysis of the effect of disorder-induced mode coupling on infrared absorption in silica. *Phys. Rev. B Condens Matter* **1998**, *38*, 1255–1273. [[CrossRef](#)]
20. Lee, J.H.; Jeong, C.H.; Lim, J.T.; Zavaleyev, V.A.; Kyung, S.J.; Yeom, G.Y. SiO_xN_y thin film deposited by plasma enhanced chemical vapor deposition at low temperature using HMDS-O₂-NH₃-Ar gas mixtures. *Surf. Coat. Technol.* **2007**, *201*, 4957–4960. [[CrossRef](#)]
21. Katumba, G.; Mwakikunga, B.W.; Mothibinyabe, T.R. FTIR and raman spectroscopy of carbon nanoparticles in SiO₂, ZnO and NiO matrices. *Nanoscale Res. Lett.* **2008**, *3*, 421. [[CrossRef](#)]
22. Liu, D.S.; Wu, C.Y. Adhesion enhancement of hard coatings deposited on flexible plastic substrates using an interfacial buffer layer. *J. Phys. D Appl. Phys.* **2010**, *43*, 175301. [[CrossRef](#)]
23. Zhang, P.; Chen, K.; Lin, Z.; Dong, H.; Li, W.; Xu, J.; Hunag, X. The role of N–Si–O bonding configurations in tunable photoluminescence of oxygenated amorphous silicon nitride films. *Appl. Phys. Lett.* **2015**, *106*, 231103. [[CrossRef](#)]

24. Kim, S.K.; Kim, Y.S.; Choi, Y.M.; Choi, J.W.; Hong, J.; Shon, J.M.; Sung, T.H.; No, K.S. Optical properties of thin amorphous silicon film on a phase shift mask for 157 nm lithography. *Jpn. J. Appl. Phys.* **2004**, *43*, 2523–2529. [[CrossRef](#)]
25. Morent, R.; De Geyter, N.; Van Vlierberghe, S.; Dubruel, R.; Leys, C.; Gengembre, L.; Schache, E.; Payen, E. Deposition of HMDSO-based coatings on PET substrates using an atmospheric pressure dielectric barrier discharge. *Prog. Org. Coat.* **2009**, *64*, 304–310. [[CrossRef](#)]
26. Choi, W.K.; Koh, S.K.; Jung, H.J. X-ray photoelectron spectroscopy studies of modified surfaces of α -Al₂O₃, SiO₂, and Si₃N₄ by low energy reactive ion beam irradiation. *J. Vac. Sci. Technol. A* **1999**, *17*, 3362–3367. [[CrossRef](#)]
27. Yu, T.; Jin, C.G.; Yang, Y.; Zhuge, L.J.; Wu, X.M.; Wu, Z.F. Effect of NH₃ plasma treatment on the interfacial property between ultrathin HfO₂ and strained Si_{0.65}Ge_{0.35} substrate. *J. Appl. Phys.* **2013**, *113*, 044105. [[CrossRef](#)]
28. Iwase, Y.; Horie, Y.; Daiko, Y.; Honda, S.; Iwamoto, Y. Synthesis of a novel polyethoxysilsesquiazane and thermal conversion into ternary silicon oxynitride ceramics with enhanced thermal stability. *Materials* **2017**, *10*, 1391. [[CrossRef](#)]
29. Fouquet-Parry, V.; Paumier, F.; Guittet, M.J.; Gautier-Soyer, M.; Satet, R.; Hoffmann, M.J.; Becher, P.F.; Painter, G.S. Composition and local bonding in RE–Si–M–O–N (M = Mg, Al; RE = La, Lu) glasses. *Appl. Surf. Sci.* **2008**, *254*, 4665–4670. [[CrossRef](#)]
30. Bertóti, I.; Tóth, A.; Mohai, M.; Szépvölgyi, J. Chemical structure and mechanical properties of Si-containing a–C:H and a–C thin films and their Cr- and W-containing derivatives. *Surf. Coat. Technol.* **2011**, *206*, 630–639. [[CrossRef](#)]
31. Castaldi, L.; Kurapov, D.; Reiter, A.; Shklover, V.; Patscheider, J. Tuning the crystallographic and electronic properties of chromium oxynitride films. *J. Appl. Phys.* **2011**, *109*, 053720. [[CrossRef](#)]
32. Zhang, Y.; Zhuang, Y.; Shen, H.; Chen, X.; Wang, J. A super hydrophilic silsesquioxane-based composite for highly selective adsorption of glycoproteins. *Microchim. Acta* **2017**, *184*, 1037–1044. [[CrossRef](#)]
33. Liang, J.; Chen, S.; Zou, C.; Tian, C.; Wang, Z.; Liao, S. Influence of oxygen contents on the microstructure, high temperature oxidation and corrosion resistance properties of Cr–Si–O–N coatings. *Coatings* **2018**, *8*, 19. [[CrossRef](#)]
34. Lin, Y.S.; Hu, C.H.; Hsiao, C.A. Enhanced scratch resistance of flexible carbon fiber-reinforced polymer composites by low temperature plasma-polymerized organosilicon oxynitride: The effect of nitrogen addition. *Compos. Sci. Technol.* **2011**, *71*, 1579–1586. [[CrossRef](#)]
35. El-Nahal, I.M.; El-Shetary, B.A.; Mustafa, A.E.B.; El-Ashgar, N.M.; Livaged, J.; Chehimi, M.M.; Roberts, A. Structural characterization of immobilized-polysiloxaneiminobis (N-diethylenediamineacetamide) ligand system. *Solid State Sci.* **2003**, *5*, 1395–1406. [[CrossRef](#)]
36. Audiffred, M.; Elías, A.L.; Gutiérrez, H.R.; López-Urías, F.; Terrones, H.; Merino, G.; Terrones, M. Nitrogen-silicon heterodoping of carbon nanotubes. *J. Phys. Chem. C* **2013**, *117*, 8481–8490. [[CrossRef](#)]
37. Howells, D.G.; Henry, B.M.; Madocks, J.; Assemder, H.E. High quality plasma enhanced chemical vapour deposited silicon oxide gas barrier coatings on polyester films. *Thin Solid Films* **2008**, *516*, 3081–3088. [[CrossRef](#)]
38. da Silva Sobrinho, A.S.; Czeremuskin, G.; Latrèche, M.; Dennler, G.; Wertheimer, M.R. A study of defects in ultra-thin transparent coatings on polymers. *Surf. Coat. Technol.* **1999**, *116–119*, 1204–1210. [[CrossRef](#)]
39. Wu, D.S.; Lo, W.C.; Chiang, C.C.; Lin, H.B.; Chang, L.S.; Horng, R.H.; Huang, C.L.; Gao, Y.J. Plasma-deposited silicon oxide barrier films on polyethersulfone substrates: Temperature and thickness effects. *Surf. Coat. Technol.* **2005**, *197*, 253–259. [[CrossRef](#)]
40. Babayan, S.E.; Jeong, J.Y.; Schütze, A.; Tu, V.J.; Moravej, M.; Selwyn, G.S.; Hicks, R.F. Deposition of silicon dioxide films with a non-equilibrium atmospheric-pressure plasma jet. *Plasma Sources Sci. Technol.* **2001**, *10*, 573–578. [[CrossRef](#)]
41. Xu, C.H.; Qin, X.M.; Guo, W.H.; Li, Y. Protrusion and whisker growth on tin coated copper substrate under stresses. *Mater. Sci. Technol.* **2011**, *27*, 1271–1274. [[CrossRef](#)]
42. Suo, Z.; Ma, E.Y.; Gleskova, H.; Wagner, S. Mechanics of rollable and foldable film-on-foil electronics. *Appl. Phys. Letts.* **1999**, *74*, 1177–1179. [[CrossRef](#)]



© 2019 by the authors. Licensee MDPI, Basel, Switzerland. This article is an open access article distributed under the terms and conditions of the Creative Commons Attribution (CC BY) license (<http://creativecommons.org/licenses/by/4.0/>).